Research article

Qiang Zhang, Danjun Liu, Qun Ren, Nicolae C. Panoiu, Li Lin, Jian Ye, Yang Huang, Shao-Ding Liu, Chi Wah Leung and Dangyuan Lei*

Probing electron transport in plasmonic molecular junctions with two-photon luminescence spectroscopy

https://doi.org/10.1515/nanoph-2021-0116
Received March 19, 2021; accepted May 17, 2021;
published online June 9, 2021

Abstract: Plasmonic core–molecule–shell (CMS) nanojunctions provide a versatile platform for studying electron transport through conductive molecules under light excitation. In general, the impact of electron transport on the near-field response of CMS nanojunctions is more prominent than on the far-field property. In this work, we use two-photon luminescence (TPL) spectroscopy to probe the effect of electron transport on the plasmonic properties of gold CMS nanojunctions. Theoretical calculations show that the TPL response of such nanojunctions is closely related to the near-field enhancement inside the metal regions, and can be strongly affected by the electron transport through the embedded molecules. TPL excitation spectroscopy results for three CMS nanojunctions (0.7, 0.9 and 1.5 nm junction widths) reveal no perceivable contribution from their low-energy plasmon modes. This observation can be well explained by a quantum-corrected model, assuming significant conductance for the molecular layers and thus efficient charge transport through the junctions. Furthermore, we explore the charge transport mechanism by investigating the junction width dependent TPL intensity under a given excitation wavelength. Our study contributes to the field of molecular electronic plasmonics through opening up a new avenue for studying quantum charge transport in molecular junctions by nonlinear optical spectroscopy.

Keywords: electron transport; molecular electronic plasmonics; molecular junctions; two-photon luminescence spectroscopy.

1 Introduction

As a promising solution for further miniaturization of electronic devices towards the sub-nanometer scale, molecular electronics has experienced a rapid growth over the past decade [1, 2]. One of the fundamental goals of molecular electronics is to clarify the electron transport mechanisms at the molecular length scale, as it is markedly different from that in macroscopic and mesoscopic electrical elements. In this respect, scanning tunneling microscopy and atomic force microscopy break junctions are the most widely used test-beds [3, 4]. In these schemes, applying a DC bias across a metal–molecule–metal junction allows for different ways of electrical characterizations, including inelastic electron tunneling spectroscopy [5], temperature–length–variable transport measurement [6, 7] and transition voltage spectroscopy [8]. Those measurements have shown that the most common electron transport mechanisms are probably coherent tunneling (including direct tunneling and Fowler–Nordheim tunneling) and incoherent hopping [1, 2]. In spite of this

***Corresponding author: Dangyuan Lei**, Department of Materials Science and Engineering, City University of Hong Kong, 83 Tat Chee Avenue, Kowloon, Hong Kong 999077, China,
E-mail: dangylei@cityu.edu.hk. https://orcid.org/0000-0002-8963-0193
Qiang Zhang and Shao-Ding Liu, Department of Physics and Optoelectronics, and Key Lab of Advanced Transducers and Intelligent Control System of Ministry of Education, Taiyuan University of Technology, Taiyuan 030024, China
Danjun Liu and Chi Wah Leung, Department of Applied Physics, The Hong Kong Polytechnic University, Hung Hom, Kowloon, Hong Kong 999077, China
Qun Ren, Department of Electronic and Electrical Engineering, University College London, Torrington Place, WC1E 7JE, London, UK; and School of Electrical and Information Engineering, Tianjin University, Tianjin, 300072, China. https://orcid.org/0000-0001-6009-4502
Nicolae C. Panoiu, Department of Electronic and Electrical Engineering, University College London, Torrington Place, WC1E 7JE, London, UK
Li Lin and Jian Ye, State Key Laboratory of Oncogenes and Related Genes, School of Biomedical Engineering, Shanghai Jiao Tong University, Shanghai 200030, China
Yang Huang, School of Science, Jiangsu Provincial Research Center of Light Industrial Optoelectronic Engineering and Technology, Jiangnan University, Wuxi 214122, China

commonly accepted view, we are still far from fully understanding the rich electron transport behaviours in molecular junctions, because other transport mechanisms exist and many quantum mechanical effects, such as quantum interference [9] and Kondo resonance [10], may also involve in the electron transport process.

At around the same time, another research field called quantum plasmonics has attracted much attention in nanophotonics [11–15]. Quantum plasmonics deals with the non-classical optical properties of metallic nanostructures caused by quantum mechanical effects, such as wave–particle duality of plasmon–polaritons, spatial nonlocality and quantum tunneling, to name a few [11–13]. Quantum plasmonics also studies ultra-strong and enhanced light–matter interactions at atomic scale, for example room-temperature strong coupling between plasmons and excitons in two-dimensional materials coupled nanocavities [16]. These quantum effects may dominate in metallic nanostructures with feature sizes on the same order of the length scale where molecular electronics operates, i.e. ranging from a few nanometers down to sub-nanometer range. Among these structures, plasmonic nanocavities fabricated by the molecular self-assembly technique have similar configurations as that of metal–molecular–metal junctions applied in molecular electronics [17]. From this point of view, it is natural to combine quantum plasmonics and molecular electronics, leading to the birth of the field referred to as molecular electronic plasmonics or plasmonic molecular electronics, a research area that has become a cutting-edge topic in nanoscience and nanotechnology [18, 19]. On the one hand, molecular electronic plasmonics concentrates on utilizing electron transport through molecules to tune the optical response of plasmonic nanostructures at the quantum size scale. On the other hand, plasmonic metal–molecule–metal nanojunctions provide an excellent platform for exploring high-frequency charge transport mechanisms with various optical spectroscopic techniques. It should be emphasized that the electron transport behaviours in plasmonic molecular nanojunctions under an optical field excitation could be more sophisticated than that revealed by electrical characterizations under a DC bias [2]. The optical field not only provides an AC bias but also, more importantly, excites plasmons in metals and electronic resonances associated with molecular optical transitions. Therefore, multiple effects influencing the electron transport in molecules have to be considered in plasmonic molecular nanojunctions, including photon-assisted electron tunneling [20], optical transitions inside the molecules [21], plasmon-induced hot electrons [22], and local heating [23–25].

So far, several far-field optical characterization methods, such as dark-field scattering and UV–Vis absorption spectroscopies, and electron energy-loss spectroscopy (EELS) have been applied to probe the electron transport effects in plasmonic metal–molecule–metal nanojunctions [26–29]. The occurrence of electron transport has been confirmed by the observation of a blue-shifted bonding dipolar resonance and a charge transfer mode (CTM) in the far-field optical spectra of the nanojunction [29–32]. For example, Tan et al. [33] used the EELS to study quantum plasmon resonance in cubic silver–molecule–silver nanojunctions, and observed the CTM at the junctions with relatively long (>1 nm) but highly conductive molecules. Nevertheless, in other configurations of such nanojunctions, electron transport does not necessarily give rise to a CTM, but leads to the quenching of some plasmon modes that originally exist in the junctions. This is typically the case for plasmonic core–molecule–shell (CMS) nanojunctions in which the molecules are embedded inside metallic nanoparticles [34–39]. Indeed, several recent studies have shown that the low-energy mode (LEM) of a gold CMS nanojunction disappears when the electron transport between the metal core and the metal shell is prominent [38, 40–42]. Although in principle the absence of LEM can also be inspected via far-field spectroscopic measurements, sometimes such measurements are not particularly robust. Instead, the LEM-associated near-field enhancement can be quite significant, making it more appropriate to study the electron transport in plasmonic nanojunctions by near-field spectroscopy techniques, such as surface-enhanced Raman spectroscopy (SERS) and nonlinear harmonic generation [43–46].

In this work, we show that the electron transport through molecular plasmonic junctions has strong impact on the two-photon luminescence (TPL) emissions of such nanojunctions. We first present a holistic theoretical and numerical investigation on the TPL response of gold CMS junctions with different junction widths. A quantum-corrected model (QCM) treating junction conductance in different ways is adopted in the numerical calculations. In experiment, we synthesize gold CMS nanojunctions with three types of conductive molecules having 1–3 benzene rings all ended with thiol groups. The comparison between TPL excitation spectroscopy results and the corresponding numerical results shows that the electron transport effect dramatically impairs the LEM-induced TPL enhancement. In the end, we numerically demonstrate the possibility of discerning different electron transport mechanisms by inspecting the junction width-dependent TPL intensities of the CMS junctions at the same excitation wavelength.

Our results illustrate a feasible means to study the electron transport mechanisms at optical frequencies and could contribute to developing optical molecular devices such as molecular optical rectifiers and switches.

2 Experimental section

2.1 Preparation of CMS nanojunctions

The 20 nm gold cores were firstly synthesized by the seed-mediated method. The obtained CTAC-capped gold cores were washed once and re-dispersed in water. The molecule powder was dissolved in ethanol. Then 50 μL of molecule ethanol solution (1 mM) were slowly added to the 1 mL of gold core (1 nM) colloids under vigorous ultra-sonication. The mixtures were then incubated for different time durations of 0.5, 3 and 9 h, for samples with BDT, BPDT, and TPDT molecules, respectively. After that, the molecule-modified gold cores were centrifuged and washed by water to remove excess molecules. The gold core–shell nanoparticles were prepared by adding 190 μL of molecule-modified core colloids into the aqueous mixture of 4 mL CTAC solution (0.1 M), 200 μL of ascorbic acid (0.04 M), and 200 μL of $HAuCl_4$ (4.86 mM). Finally, the obtained gold CMS junctions were washed and kept in CTAC solution. Then, these synthesized gold CMS junctions with different molecular junctions were washed by centrifugation and then re-dispersed in H_2O before drop-casting onto the glass substrate and subsequently dried in air at room temperature to do the optical characterization [47]. The refractive indices of the BDT and BPDT (TPDT) molecular layers were quantified as 1.59 and 1.65 (1.65), respectively, by fitting experimental and calculated shifts of plasmon resonance of the nanoparticles using the least squares method [48].

2.2 Dark-field spectroscopy

Optical dark-field imaging and spectroscopy were performed on a customized Olympus BX51 microscope. A 100× dark-field objective (LMPlanFLN-BD, NA = 0.8) was used to focus an un-polarized white-light beam from an incandescent lamp onto the sample plane. Scattered light was collected through the same objective and analyzed with an imaging spectrometer (Acton SP2300, Princeton Instruments) equipped with a gray CCD camera (PIXIS: 400BR eXcelon, Princeton Instruments).

2.3 Experimental TPL characterization of gold CMS nanojunctions

TPL emissions from individual CMS nanojunction were measured on a commercial laser scanning confocal microscope system (TCS SP8, Leica) coupled with a Ti:Sapphire femtosecond laser (Mai Tai HP, Spectra-Physics). The pulse duration and repetition rate of the laser pulse are about 100 fs and 80 MHz, respectively. The excitation power was kept at about 5 mW in all the TPL measurements. The linewidths of the pump laser at different excitation wavelengths were measured by a fiber spectrometer (BroLight). The laser beam was tightly focused by a 100× dry objective with a high NA of 0.95. The scanning of the laser beam at the focal plane was controlled by a scan field rotation module. While scanning over the sample, TPL emission signals were detected simultaneously by a HyD detector.

2.4 Numerical simulations

Full-wave electromagnetic simulations were performed by COMSOL Multiphysics based on finite element method. Permittivity of gold was taken from the empirical data given by Johnson and Christy [49]. Experimentally measured real parts of the refractive index of molecular junctions were used in the simulation, where the index of refraction of BDT molecular junction was set to 1.59, and that of BPDT and TPDT molecular junctions was equal to 1.65. A semi-infinite thick glass substrate was adopted in the simulation with a predefined background field obtained by using Fresnel formulas for a glass–air interface. The whole computation domain was surrounded by a perfectly matched layer (PML) to eliminate unphysical reflections at the boundaries. The meshes of all the simulation models were fine enough to reach the convergence of the computation.

3 Results and discussion

3.1 Numerical investigation of linear and TPL responses of gold CMS nanojunctions

Linear optical response of gold CMS junctions has been extensively studied both numerically and experimentally [34, 37–39]. Based on these studies, the optical resonances of a gold CMS nanojunction can be understood as the hybridization between the plasmon modes sustained by the outer gold shell and the inner gold core [38–42, 44]. In this description, the distance between the shell and the core, i.e. the junction width, is one of the most important factors that determine the resonant features of a gold CMS junction, such as the resonant wavelength, scattering cross-section and near-field enhancement.

To begin with, we first investigate the linear optical response of a gold CMS nanojunction with junction width varying from 0.7 to 10 nm when the radii of the inner core (r_1) and the outer shell (r_2) are kept as 10 and 30 nm, respectively (see the inset in Figure 1a). For simplicity, here the gold CMS nanojunction is assumed to be free-standing in air and an insulating junction is considered by setting the refractive index of the medium in the gap between the shell and the core to 1.60. A code implementing the Mie scattering theory is used to compute both the far-field and near-field optical response of the gold CMS insulating junction under the excitation with a linearly polarized plane wave [50].

Figure 1a shows the map of the normalized extinction cross section of the gold CMS insulating nanojunction as a function of the junction width in the wavelength range of

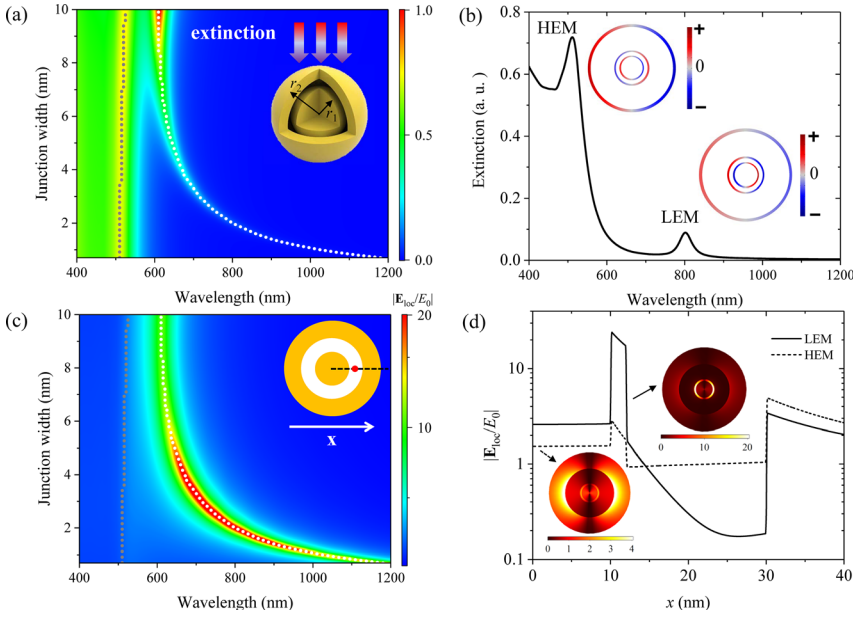

Figure 1: Linear optical responses of the gold core–molecule–shell (CMS) insulating junction as a function of the junction width varying from 0.7 to 10 nm.

(a) Normalized extinction cross section as a function of the junction width in the wavelength range of 400–1200 nm. The gold CMS junction is assumed to be free standing in air and excited by a linearly polarized plane wave. The gray (white) dotted-line guides the wavelength of the maximum extinction of the high (low) energy band as a function of the junction width. (b) Spectrum of the normalized extinction cross section of the gold CMS junction with 2 nm width. The insets close to the extinction peaks illustrate the corresponding transient surface charge distribution on the metal surfaces at the low-energy mode (LEM) and high-energy mode (HEM). (c) Near-field enhancement factor $|\mathbf{E}_{loc}/E_0|$ monitored at the junction centre as a function of the junction width in the wavelength range of 400–1200 nm. The inset shows the monitoring point (red dot) and the *x*-coordinate. (d) Near-field enhancement factor $|\mathbf{E}_{loc}/E_0|$ of the gold CMS junction with 2 nm width along the *x*-coordinate from the centre to the edge of the gold CMS junction as marked by the black dashed line in the inset in (c). The solid and dashed lines correspond to the LEM and HEM, respectively.

400–1200 nm. It is seen that there are two distinct resonance bands whose spectral features have quite different dependence on the junction width. The wavelength of the high-energy band is about 515 nm and barely varies with the junction width (gray dotted-line). In addition, the extinction cross-section of this high-energy band is also only weakly dependent on the junction width. On the contrary, as the junction width increases, the resonance wavelength of the low-energy band is increasingly blue-shifted whereas the corresponding extinction cross-section increases (white dotted-line). Figure 1b shows the extinction spectrum of the gold CMS junction with a particular junction width (2 nm). The resonance peak at 515 nm corresponds to a high-energy mode (HEM) while the one at 800 nm is a low-energy mode (LEM). The surface charge distributions on the metal surface of the LEM and the HEM are given in the corresponding insets located close to the extinction peaks. Notice that for the HEM (LEM) the charge density on the exterior surface of the gold CMS junction is larger (much smaller) than that on the interior surfaces (the inner surface of the shell and the surface of the core). This difference explains why the optical response of the HEM is less sensitive to variations of the junction width than that of the LEM. In addition to the far-field response, in this work we are also particularly concerned with the near-field properties of the gold CMS junction because many non-linear optical processes, such as second-harmonic generation and TPL, are related to the plasmon-enhanced near-field. Figure 1c shows the near-field enhancement factor $|\mathbf{E}_{loc}/E_0|$ monitored at the centre of the junction (see the red dot in the inset) as a function of the junction width in the wavelength range of 400–1200 nm, where $\mathbf{E}_{loc}$ is the local electric field and E_0 is the amplitude of the incident plane wave. It is clearly seen that the near-field enhancement factor of the LEM in the junction region is much stronger than that of the HEM. Therefore, metallic CMS nanojunctions can serve as excellent surface-enhanced Raman tags when molecules are embedded in the gap region [36–38]. Considering the symmetry of the junction, the spatial distribution of the near-field enhancement can be simply investigated by calculating $|\mathbf{E}_{loc}/E_0|$ along the *x*-coordinate from the centre of the core ($x = 0$ nm) to 10 nm away from the outer surface of the shell ($x = 30$ nm). Figure 1d shows the spectra of $|\mathbf{E}_{loc}/E_0|$ of the LEM and HEM

for the gold CMS junction with 2 nm junction width. It shows that the strongest near-field enhancement factor of the LEM corresponds to the gap region and can be larger than 10. Moreover, it is worthy to notice that the electric fields associated with both LEM and HEM inside the gold core can also be enhanced, though the enhancement factors are smaller than that inside the junction. However, this weak near-field enhancement in the metal region is crucial for some bulk absorption related nonlinear optical processes, for example, the plasmon-assisted TPL emission. Based on the physical picture of the plasmon associated TPL emission (see Supporting Information for the details), the TPL emission intensity from an infinitesimal volume dV of a plasmonic nanoparticle can be obtained as [51–55]:

$$I_{\mathrm{TPL}}(\omega_{\mathrm{em}},\mathbf{r})\cdot dV = I^2(\omega_{\mathrm{ex}},\mathbf{r})\cdot Y_{2\mathrm{abs}}(2\omega_{\mathrm{ex}})\cdot Y_{\mathrm{r}}(\omega_{\mathrm{em}}) \cdot Y_{\mathrm{em}}(\omega_{\mathrm{em}})\cdot dV \quad (1)$$

Here, ω_{em} (ω_{ex}) is the angular frequency of the emission (excitation), $I(\omega_{\mathrm{ex}},\mathbf{r})$ denotes the excitation intensity at position $\mathbf{r}$, $Y_{2\mathrm{abs}}(2\omega_{\mathrm{ex}})$ is the absorption probability of two photons for generating energetic electron–hole pairs with energy of $2\hbar\omega_{\mathrm{ex}}$, $Y_{\mathrm{r}}(\omega_{\mathrm{em}})$ is the relaxation probability of the energetic electron–hole pairs to the emission energy, and $Y_{\mathrm{em}}(\omega_{\mathrm{em}})$ is the emission probability corresponding to the radiative recombination in bulk metals but modified by the plasmonic antenna effect. In Equation (1), both $Y_{2\mathrm{abs}}(2\omega_{\mathrm{ex}})$ and $Y_{\mathrm{r}}(\omega_{\mathrm{em}})$ are determined by the intrinsic property of the metal. The excitation intensity $I(\omega_{\mathrm{ex}},\mathbf{r})$ is equal to $|\mathbf{E}_{\mathrm{loc}}(\omega_{\mathrm{ex}},\mathbf{r})|^2$, where $\mathbf{E}_{\mathrm{loc}}(\omega_{\mathrm{ex}},\mathbf{r})$ is the local electric field at ω_{ex} and position $\mathbf{r}$. The plasmon-modified emission probability $Y_{\mathrm{em}}(\omega_{\mathrm{em}})$ is essentially related to the local density of plasmonic states, which is proportional to the local field intensity at ω_{em}, i.e. $|\mathbf{E}_{\mathrm{loc}}(\omega_{\mathrm{em}},\mathbf{r})|^2$. Going back to Figure 1d, we can conclude that the near-field enhancement of the LEM inside the metal region contributes to the enhancement of $I(\omega_{\mathrm{ex}},\mathbf{r})$, whereas the HEM excitation increases the photon emission at short wavelengths, thus increasing $Y_{\mathrm{em}}(\omega_{\mathrm{em}})$. Equation (1) can be further reduced to Equation (2) by dropping $Y_{2\mathrm{abs}}(2\omega_{\mathrm{ex}})$ and $Y_{\mathrm{r}}(\omega_{\mathrm{em}})$ when we are only concerned about the relative TPL intensity of particles with the same metal composition (see Supporting Information):

$$I_{\mathrm{TPL}}^{\mathrm{rel}}(\omega_{\mathrm{em}},\mathbf{r})\cdot dV \propto L_{\mathrm{ex}}(\omega_{\mathrm{ex}},\mathbf{r})\cdot L_{\mathrm{em}}(\omega_{\mathrm{em}},\mathbf{r})\cdot dV \quad (2)$$

In Equation (2), $L_{\mathrm{ex}}(\omega_{\mathrm{ex}},\mathbf{r}) = |\mathbf{E}_{\mathrm{loc}}(\omega_{\mathrm{ex}},\mathbf{r})/E_0|^4$ and $L_{\mathrm{em}}(\omega_{\mathrm{em}},\mathbf{r}) = |\mathbf{E}_{\mathrm{loc}}(\omega_{\mathrm{em}},\mathbf{r})/E_0|^2$ are the near-field enhancement factors at the excitation and emission wavelength, respectively. Equation (2) is then integrated over the volume V that is the metal part of the CMS nanojunction, and the spatially averaged relative TPL intensity can be finally obtained after dividing the integration by V.

Using Equation (2), we can numerically study the TPL response of gold CMS nanojunctions. Hereinafter, all the geometries and material properties of the simulation models are chosen so as to accurately describe the synthesized samples in the experiments that will be discussed later. To be more specific, the radii of the outer shell and the inner core of the gold CMS junctions are kept as 30 and 10 nm, respectively. In addition, gold CMS nanojunctions are placed on a glass substrate in simulations to be consistent with the experiments.

We first consider the configurations with insulating dielectric junctions of three different widths, namely 0.7, 0.9 and 1.5 nm. The refractive index for the 0.7 nm junction is set to 1.59, and that for 0.9 and 1.5 nm junctions is 1.65. For comparison, the TPL response of a solid gold nanosphere of 30 nm in radius is also calculated. Figure 2a shows the spectra of the relative TPL intensity of the gold nanosphere and the gold CMS nanojunctions excited by a linearly polarized plane wave with amplitude E_0 and wavelength 750 nm. Clearly, all the spectra show a TPL emission peak near 525 nm in the emission wavelength (λ_{em}) ranging from 400 to 650 nm. This confirms that the TPL emission of the gold CMS nanojunction is enhanced by the plasmonic antenna effect of the HEM, red-shifted to 525 nm due to the presence of the substrate. For the gold nanosphere, the TPL emission peak is attributed to the electric-dipole mode whose resonance wavelength is very close to that of the HEM of the gold CMS nanojunction. For the gold CMS nanojunction, we find that the TPL response depends on the junction width. For example, the TPL intensity of the gold CMS junction with 2 nm junction width is overall larger than that of the other junctions with smaller width. Additional calculations of the gold CMS insulating nanojunction excited at other wavelengths (see Figure S2 in Supplementary material) indicate that the TPL intensity is also enhanced by the LEM, whose resonance wavelength depends on the junction width, too. In Figure 2b we compare the TPL intensity of the gold CMS nanojunctions and the solid gold nanosphere, integrated in the emission wavelength range of 400–650 nm, as a function of the excitation wavelength (λ_{ex}). Similarly, the integrated TPL intensity of gold CMS junctions with different junction widths shows peaks at the resonance wavelengths of the LEMs while that of a solid gold nanosphere without the LEM monotonously decreases in the excitation wavelength ranging from 700 to 1200 nm. Therefore, it is clear that the spectral position and near-field enhancement factor of the LEM determine the dependence of the integrated TPL intensity as a function of λ_{ex}.

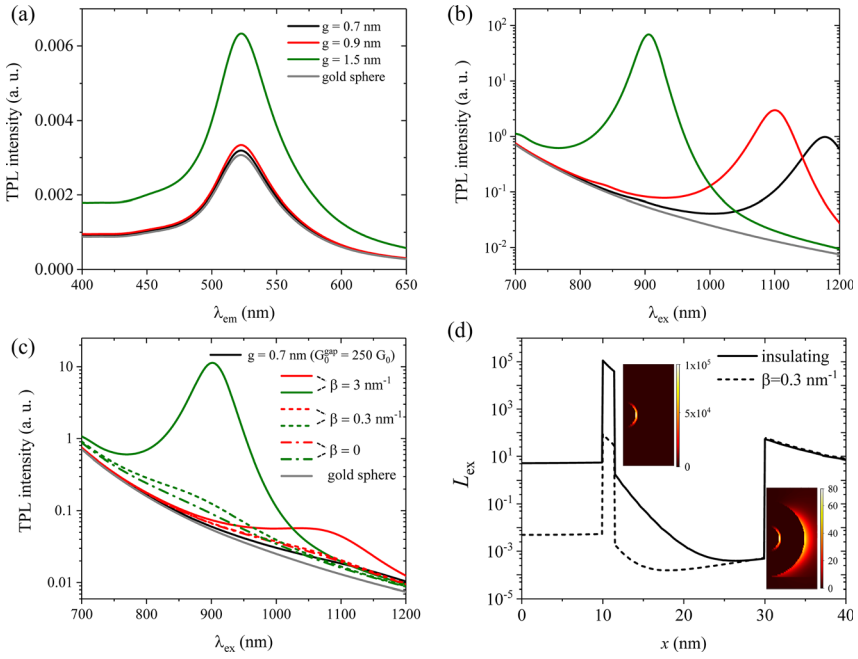

Figure 2: Calculated two-photon luminescence (TPL) responses of gold core–molecule–shell (CMS) nanojunctions with junction width (denoted as g) of 0.7, 0.9 and 1.5 nm based on different models of the junction conductance.
(a) Relative TPL intensity of gold CMS nanojunctions as a function of the emission wavelength (λ_{em}) excited at 750 nm calculated based on a classical dielectric junction model. (b) Integrated TPL intensity as a function of the excitation wavelength (λ_{ex}) calculated based on the same model as used in (a). (b) Shares the same legend as (a). (c) Integrated TPL intensity as a function of the excitation wavelength (λ_{ex}) calculated based on the tunneling-type model. TPL intensity of a solid gold sphere is plotted in (a)–(c) by the gray line. Note that the results corresponding to $g = 0.7$ nm for different β are the same as shown by the black solid line. (d) Near-field enhancement factor (L_{ex}) from the centre to 10 nm away from the outer shell of the gold CMS junction calculated at the excitation wavelength of the LEM based on the insulating model (solid line) and the tunneling-type model with $\beta = 0.3$ nm^{-1} (dashed line). The left and right insets show the distribution of L_{ex} across the middle cross-section of the gold CMS junction.

After discussing the linear and TPL responses of gold CMS junctions with simple dielectric junctions, we are now in a position to find out how charge transport in the nanojunction affects the TPL response of the gold CMS junction. From a computational point of view, the junction in the gold CMS junction must be treated as a conductive material with a complex dielectric function when charges can flow across it. This is exactly the principle of the quantum-corrected model (QCM) that has been frequently used in recent studies of charge transfer effects in plasmonic nanostructures [29–31, 56]. Based on the QCM, the relative permittivity of the conductive gap ϵ_{gap} is written as [28, 33, 38, 44]:

$$\epsilon_{gap} = n_d^2 + \frac{i\sigma_{gap}}{\omega\epsilon_0}, \tag{3}$$

where n_d is the real part of the refractive index, i is the imaginary unit, and ϵ_0 is the permittivity of the vacuum. The key parameter in Equation (3) is the conductivity σ_{gap}, which is related to the junction conductance G_{gap}. By deriving the resistance (R_{gap}) of a spherical shell junction with inner radius r_1 and width g and using the relationship $G_{gap} = 1/R_{gap}$, it is easy to obtain [44]:

$$G_{gap} = \frac{\sigma_{gap} \cdot 4\pi r_1 (r_1 + g)}{g}, \tag{4}$$

where g denotes the junction width. If we consider the junction in the gold CMS junction as a macroscopic electrical circuit element, σ_{gap} should be a constant for different junction widths, because the conductivity is an intrinsic material property, and thereby it should not depend on the system geometrical configuration. In this classical circuit model, G_{gap} is approximately proportional to $1/g$, as per Equation (4). But at molecular scale, electrons (holes) transport obeys the laws of quantum mechanics, and tackling the accurate dependency of G_{gap} on the junction width needs the aid of some first-principle methods, for example, time-dependent density function theory [56, 57]. Therefore, we conclude that although the QCM can be used in a classical electromagnetic simulation, σ_{gap} in Equation (3) is related to the molecular conductance G_{gap} that is ultimately determined by the quantum charge transport.

In general, when the electrons transport follows the quantum tunneling-type mechanism such as direct tunneling and indirect hopping G_{gap} exponentially decreases as the junction width increases [1, 2, 18, 58–61]:

$$G_{gap}(g) = G^0_{gap}\exp[-\beta\cdot(g-g_0)], \quad (5)$$

where G^0_{gap} is the conductance of the shortest junction with the width g_0 and β is the decay factor. In our samples, the shortest CMS junctions are embedded with BDT molecules, i.e. g_0 = 0.7 nm. In the following numerical calculations, G^0_{gap} is assumed to be 250 times larger than the quantum conductance G_0 (7.745×10^{-5} S). This assumption is based on the conductance of a single 1,4-benzenedithiol (BDT) molecule, which in our previous study was estimated to be equal to 0.044 G_0 [44].

Many studies indicate that β is primarily determined by two factors: Barrier height and the charge transport mechanism [1]. In a direct tunneling process, the barrier height of a metal–molecule–metal junction depends on the offset between the Fermi level of the metal and the energy levels of the molecular frontier orbitals (HOMO or LUMO). Note that direct tunneling through a molecular junction shares a physical picture similar to quantum tunneling through a vacuum or dielectric nanogap. The main difference is that the barrier height in a metal–molecule–metal junction is usually lower than that of a metal–vacuum–metal junction, which results in smaller decay factor for the former structure. For example, β is typically in the range of 1–3 nm^{-1} for an unsaturated molecule filled junction, whereas that for a vacuum junction is typically 29 nm^{-1} [6]. When charge transport changes from direct tunneling to indirect hopping, β can be as small as 0.3 nm^{-1} [6, 61]. In Figure 2c, we show the spectra of the integrated TPL intensity as a function of the excitation wavelength ranging from 700 to 1200 nm, calculated using Equation (5) by considering three different values of β. It is seen that for a larger decay factor (β = 3 nm^{-1}), the spectra of the TPL intensity still show distinct peaks at the resonance wavelengths of LEMs for gold CMS junctions with large junction widths (g = 0.9 and 1.5 nm) although the strengths are much smaller than those calculated based on the insulating model (Figure 2b). This finding indicates that the charge transport in gold CMS junctions with large junction widths is not sufficient to completely quench the LEM because the tunneling probability with β = 3 nm^{-1} quickly decreases as the junction width increases. Nevertheless, when a more efficient charge transport occurs, for example via hopping, the decrease of the junction conductance can be much slower, yielding strong quenching of the LEM even for a large junction width. This is verified by the spectra in Figure 2c, which correspond to β = 0.3 nm^{-1} and g = 0.9 and 1.5 nm, where the peaks of the TPL intensity at the resonance wavelengths of the LEM are vanishingly small. We also consider a limiting case in which the junction conductance is independent on the junction width, i.e. β = 0. Under these circumstances, the charge transport in the molecular junction is strong enough to completely quench all the LEMs for different junction widths as shown by the dash-dotted lines in Figure 2c. In this case, the TPL response of the gold CMS junctions becomes similar to that of a solid gold nanosphere (solid gray line), which shows a monotonously decreasing trend as λ_{ex} increases from 700 to 1200 nm. In addition, if we keep σ_{gap} in Equation (3) as a constant for CMS nanojunctions with different junction widths, i.e. junctions embedded with a classical lossy metal, the results are similar to that for conductive molecules with small decay factors β = 0.3 nm^{-1} and 0 in Figure 2c (also see Figure S3 in Supplementary material). This is comprehensible because lossy metals can be highly conductive, but the dependences of the conductance on junction width in lossy metal junctions and molecular junctions are quite different (see Figure S4 in Supplementary material). In Figure 2d we compare the near-field enhancement (L_{ex}) of the LEM calculated for an insulating junction model and a molecular junction model with β = 0.3 nm^{-1}, from the centre of the core up to 10 nm away from the outer surface of the shell. This comparison shows that the near-field enhancement is markedly reduced in the gold CMS junction with a molecular junction chiefly due to the strong charge transfer effect. More interestingly, the field suppression mainly occurs inside the junction and in the metal regions close to it, whereas the field distribution outside of the shell is mostly unchanged, as shown by the distribution of L_{ex} across the middle cross-section of the gold CMS junction with an insulating (left inset) and a molecular junction (right inset). We also find that the HEM (resonance at the short wavelength) hardly depends on the nature of the charge transport, leading to the same field distributions in gold CMS junctions with an insulating and a molecular junction (see Figure S5 in Supplementary material).

3.2 Experimental characterization of the TPL response of gold CMS junctions with different molecular junctions

To experimentally corroborate the conclusions drawn from the just discussed numerical simulations, we synthesized gold CMS nanojunctions using a wet-chemistry method (see Experimental section). The nanojunctions were

formed by three kinds of molecules: 1,4-benzenedithiol (BDT), 4,4′-biphenyldithiol (BPDT) and 4,4′-terpheyldithiol (TPDT). BDT, BPDT and TPDT molecules have 1, 2 and 3 aromatic rings, respectively, with thiol groups as the anchoring groups at both ends. The structures of these molecules are shown in the top insets in Figure 3a–c, respectively. The statistically averaged junction widths of the synthesized gold CMS nanojunctions embedded with BDT, BPDT and TPDT molecules were obtained as 0.7, 0.9 and 1.5 nm, respectively. TEM images of the samples are shown in the bottom insets in Figure 3a–c, from which the radii of the gold core and the outer shell are estimated as 10 and 30 nm for all gold CMS nanojunctions.

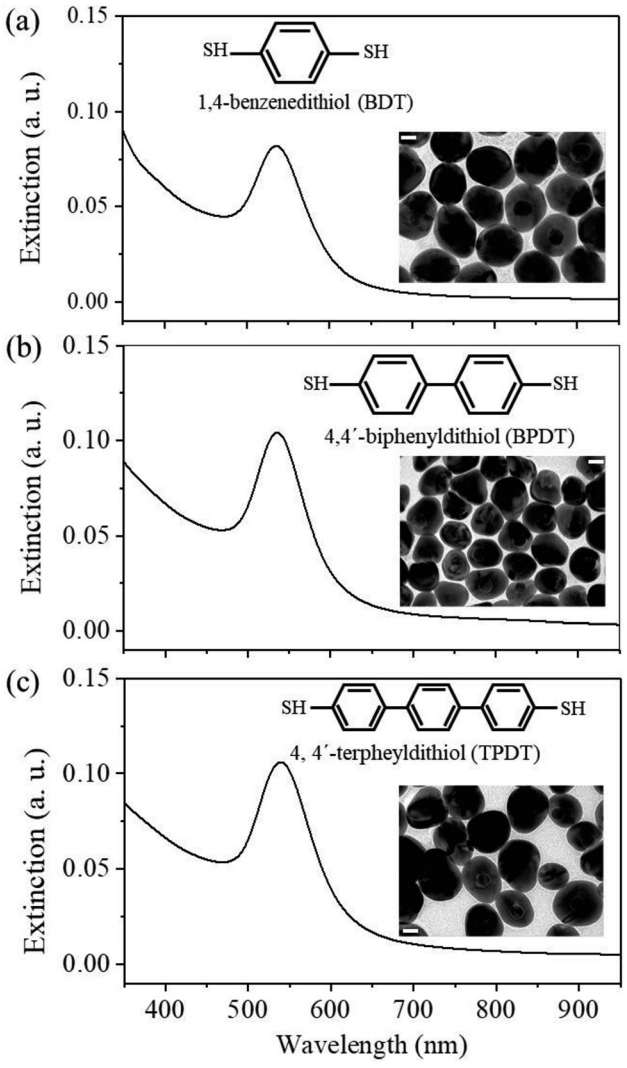

Figure 3: Far-field experimental characterization of gold CMS nanojunctions with (a) BDT, (b) BPDT and (c) TPDT molecular layers. TEM images of the samples and the molecular structures are shown in the bottom and top insets, respectively. The scale bars of the TEM images in (a)–(c) are 20 nm.

We first characterized the far-field response of the samples by measuring their UV–Vis spectra. As can be seen from Figure 3, each extinction spectrum shows a single peak of the HEM near 535 nm, whereas no spectral signature of LEMs can be identified. This observation is consistent with our previous study [38, 44], which implies that the LEMs in gold CMS nanojunctions embedded with these three kinds of molecules are quenched due to the significant charge transfer effect. However, this conclusion drawn from the far-field experimental characterization might not be reliable due to the fact that the absence of the LEM in the UV–Vis spectra may also be a consequence of the spectral suppression and broadening effects caused by the defects of measured samples and the effect of averaging over multiple particles. Therefore, exploring the near-field response of gold CMS junctions is arguably a more suitable method for probing the charge transfer effect.

Theoretical and numerical results summarized in Figures 1 and 2 indicate that TPL is another efficient optical near-field probe that can be employed to study the charge transport in CMS nanojunctions. Different from the UV–Vis spectroscopy, which measures the extinction spectra of nanoparticles in solution, the TPL experimental characterization was carried out on single nanoparticles deposited on a glass substrate. Figure 4a schematically shows our TPL measuring system based on a commercial laser scanning confocal microscope equipped with a Ti:sapphire femtosecond laser (see Experimental section). Figure 4b shows the false color image of the TPL emission of a generic sample containing gold CMS nanojunctions, exhibiting light spots of different size. We compare this non-linear emission image with the corresponding dark-field image from the same area to identify single particles for further spectra acquisition. During measurements, we ensured that the investigated particles were not damaged by the femtosecond laser illumination, meaning that both the dark-field scattering spectra and images recorded before and after the TPL characterization were not affected by these measurements (see Figure S6 in Supplementary material). The measured (symbols) and fitted (red line) TPL spectrum of a single gold CMS junction show an emission peak near 550 nm, as per Figure 4c. Here, the TPL intensity was obtained by collecting the emission from an area that covers only one particle. The area size and excitation power of the laser were the same for each type of the sample. Compared to the numerical results shown in Figure 2a, the measured TPL spectrum is clearly broader and red-shifted due to the imperfections of the synthesized samples.

Next, we experimentally study the charge transfer effect in molecular junctions by measuring the integrated TPL intensity of gold CMS nanojunctions in the emission

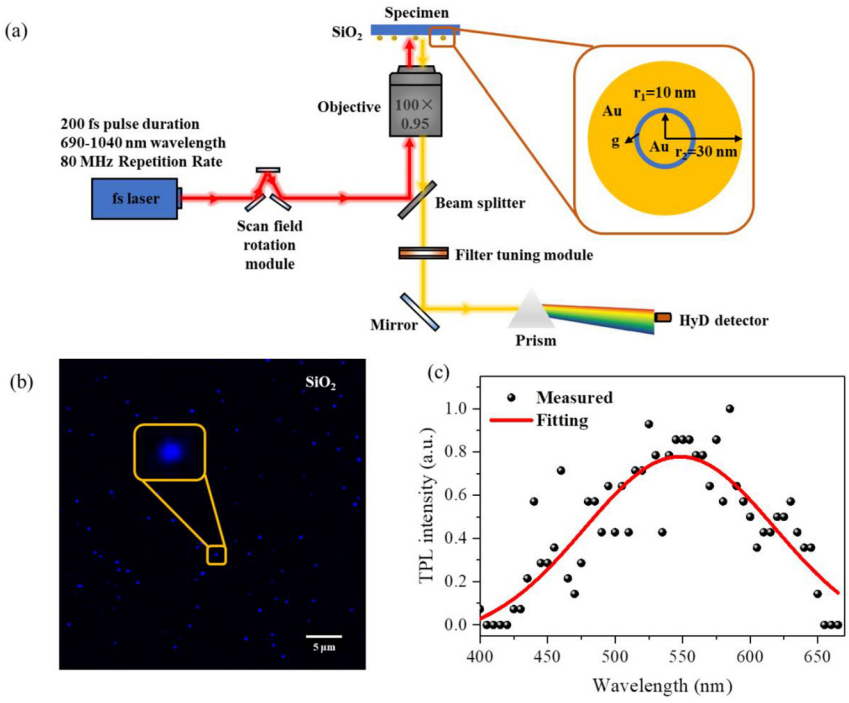

Figure 4: Experimental TPL characterization of gold CMS nanojunctions. (a) Schematic of the confocal TPL spectroscopy system. (b) TPL false color images of gold CMS nanojunctions (average 1.5 nm junction width) placed on a glass substrate. (c) Measured (symbols) and fitted (line) TPL spectra of a gold CMS nanojunction (marked by the yellow square in Figure 4b).

wavelength ranging from 400 to 650 nm, as a function of the excitation wavelength, and comparing it with the corresponding results of numerical simulations. Limited by our laser system, the wavelength of the excitation in the experiment can reliably be tuned only in the range from 715 to 800 nm. Symbols in Figure 5 show the measured TPL intensity versus the excitation wavelength, for a solid gold nanosphere, gold CMS nanojunctions with BDT, BPDT and TPDT molecules in (a)–(d), respectively. As can be seen from Figure 5, the experimental data points (symbols) have relatively large deviation errors, indicating that the measured TPL intensities at different excitation wavelengths are fluctuated to some extent. These fluctuations are mainly due to three factors. First, it is difficult to synthesize metallic CMS nanojunctions with perfectly uniform size and shape. To investigate the influence of particle size and shape on TPL intensity, we perform an exemplary calculation of the TPL intensities of spherical CMS nanojunctions with varied size and of ellipsoidal CMS junctions with the same volume. The results show that the relative TPL intensity at a specific excitation wavelength indeed varies as the size and shape of the CMS nanojunction change (see Figure S7 in Supplementary material). Second, the focus spot of the pump laser at different excitation wavelengths cannot be accurately adjusted to the same size, which may lead to wavelength-dependent excitation power density. Third, the linewidth of the pump laser varies with output wavelength (see Table S1 in Supplementary material), which also has an influence on the measured TPL intensities. Considering these reasons, we are more concerned about the variation trend of TPL intensity with excitation wavelength rather than the absolute TPL intensity value at a specific excitation wavelength. The trend in the excitation wavelength range after 700 nm is more reliable because it is predominately determined by the resonance strength of the LEM in the CMS nanojunctions, and is not likely to be changed by the fluctuation if we use statistic data. To make a fair comparison between the experimental and numerical results, the experimental data were fitted by using the errors as weight and then the fitted and numerical spectra are normalized to the intensity at 715 nm. First, we see that for a solid gold nanosphere the measured TPL intensity (solid line in Figure 5a) decreases as the excitation wavelength increases, which agrees with the trend of the numerically determined spectrum (dashed line in Figure 5a). Furthermore, for gold CMS nanojunctions with shorter junction widths (BDT and BPDT molecules), the calculated TPL intensity obtained by considering an insulating junction and a molecular junction with different values of β presents no discernible differences in the excitation wavelength range of 715–800 nm, as shown by the dashed lines in Figure 5b and c. Both the measured and calculated TPL intensity decrease as the excitation wavelength increases, which is similar to the results of a solid gold nanosphere shown in Figure 5a. This can be understood by the fact that the resonance wavelengths of LEMs of gold CMS junctions with short junction width (0.7 and 0.9 nm)

are far beyond 800 nm, as illustrated by the numerical results shown in Figure 2b. In this context, whether charge transport occurs or not cannot be concluded from the results in Figure 5b and c. Yet, for gold CMS junctions with a longer molecular layer (TPDT, 1.5 nm) the resonance wavelength of the LEM is about 900 nm (see Figure 2b), which is close to the edge of the window of the excitation wavelength range (715–800 nm) in Figure 5. As a consequence, the variation of the TPL intensity as a function of λ_{ex} is different for numerical calculations based on different models of junction conductance, as shown in Figure 5d. In short, when the junction is completely insulating (black dashed-line) or the conductance is quite small, for example in the tunneling-type model with $\beta = 3$ nm^{-1} (blue dashed-line), the TPL intensity first decreases then increases in the excitation wavelength range of 715–800 nm. Otherwise, when $\beta = 0.3$ nm^{-1} (olive dashed-line) and $\beta = 0$ (pink dashed-line), the TPL intensity decreases throughout the same excitation wavelength range. Clearly, the experimental results in Figure 5d can match the numerical ones only when highly conductive molecular junctions with slow decay factors of $\beta = 0$ and $\beta = 0.3$ nm^{-1} are considered in the simulation. Hence, we believe that the results shown in Figure 5d provide another experimental evidence of the significant charge transport in the molecular junctions. As the TPL response (Figure 5) is closely related to the near-field properties of the gold CMS junction, the conclusions it implies are more reliable than those derived from far-field investigations (Figure 2) vis-à-vis of characterizing the charge transport in molecular junction.

Finally, we want to further expand on the possibility of distinguishing between the mechanisms of the charge transport in molecular junctions by studying the TPL response of the gold CMS junctions. As a matter of fact, results in Figure 2 already show that the TPL intensity of gold CMS junctions with varying junction width as a function of the excitation wavelength depends on the model used to describe the junction conductance. So, it is possible to unravel the mechanism of the charge transport from Figure 5, at least qualitatively, if one extends the excitation wavelength of the laser to a broader range, for example, up to 1200 nm. Alternatively, one can use a fixed excitation wavelength (for example 785 nm) but study the TPL response of gold CMS junctions with varying junction width. To demonstrate this possibility numerically, in Figure 6 we calculate the peak TPL intensity of the gold CMS junction excited at 785 nm as a function of the junction

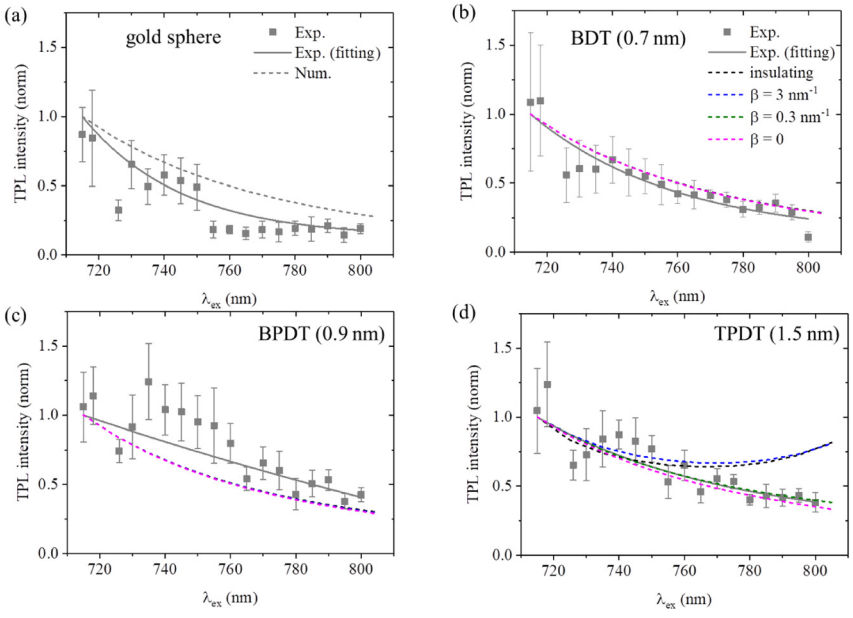

Figure 5: Comparison between the experimentally measured TPL responses of gold sphere as well as gold CMS junctions and numerical results calculated using different models. Measured (symbols) and calculated (dashed-lines) integrated-TPL intensity of (a) a solid gold sphere, gold CMS junctions with (b) BDT, (c) BPDT and (d) TPDT molecular junctions, as a function of the excitation wavelength (λ_{ex}) in the range from 715 to 800 nm. The solid lines are the fitted curves of the experimental data and (b)–(d) share the same legends. The error bars represent standard deviations of the TPL intensity of several particles at each excitation wavelength. Note that the dashed-lines in (b) and (c) are highly overlapping because the numerical results of different models of CMS nanojunctions with very small junction widths (0.7 and 0.9 nm) are almost the same in the wavelength window of 715–800 nm.

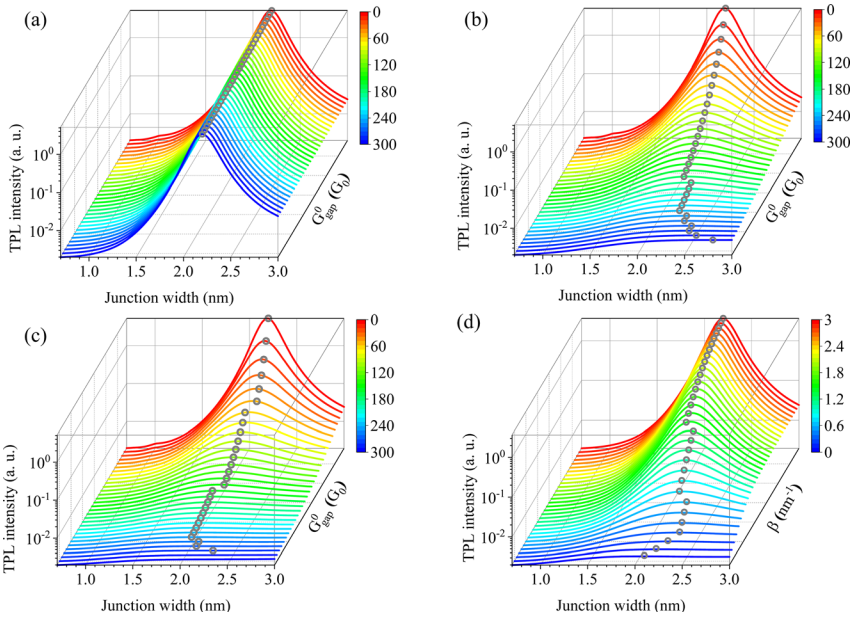

Figure 6: TPL intensity of the gold CMS junction excited at λ_{ex} = 785 nm as a function of the junction width calculated based on Equations (3)–(5) with varying parameters.
(a) Changing the initial junction conductance G^0_{gap} from 0 to 300 G_0 while keeping the decay factor β = 3 nm^{-1}. (b) and (c) are the same as (a) but with β = 0.3 nm^{-1} and 0, respectively. (d) Changing the decay factor β from 0 to 3 nm^{-1} while keeping G^0_{gap} = 250 G_0. The color bars are mapped by the values of G^0_{gap} in (a)–(c) and by the values of β in (d). The TPL intensity peak for each line is marked by the gray circle.

width from 0.7 to 3 nm based on Equations (3)–(5). As the only variables in Equation (5) are the conductance of the shortest junction (G^0_{gap}) and the decay factor β, we fix one of them and change the other one and observe the evolution of the TPL intensity. As can be seen from the results summarized in Figure 6a, where β is fixed to 3 nm^{-1}, when the junction conductance decreases steeply as the junction width increases, the evolutions of the TPL intensity as a function of the junction width for G^0_{gap} changing from 0 to 300 G_0 are nearly the same. All the spectra show a peak (marked by the gray hollow-dots) at roughly the same junction width of 2.2 nm, which actually corresponds to the resonant junction width of the LEM at 785 nm. Conversely, when the junction conductance decreases slowly, as in Figure 6b and c, where β is fixed as 0.3 nm^{-1} and 0, respectively, the way of the dependence of TPL intensity on the junction width is more strongly affected by changes of G^0_{gap}. Especially for large values of G^0_{gap}, the junction width of the peak intensity varies markedly with G^0_{gap}. Similarly, when G^0_{gap} is constant, the TPL intensity shows different dependence on the junction width for different β, as shown in Figure 6d. Therefore, it is possible to determine at least qualitatively the charge transfer mechanism (for example, direction tunneling with a large decay factor or hopping with a small decay factor) in the molecular junction, by synthesizing gold CMS nanojunctions with controllable junction width and then compare the spectra measured using TPL emission with the corresponding ones obtained via numerical calculations.

4 Conclusion

In summary, we have investigated the TPL response of gold CMS nanojunctions embedded with different molecules and found that the charge transport in the junctions has strong impact on the non-linear optical response of such quantum plasmonic systems. Theoretical and numerical results have demonstrated that the near-field enhancement of the LEM inside the metal regions is also significantly quenched due to the charge transfer effect. As a result, the TPL response of gold CMS nanojunctions with highly conductive molecules is similar to that of a solid gold nanosphere, which has been proved by both the numerical calculations and experimental measurements. We also discussed the possibility to study the charge transport mechanism across the molecules using the TPL characterization. Our results indicate that in addition to the SERS, the TPL spectroscopy can be used as efficient near-field probe to investigate the charge transport mechanisms in plasmonic molecular nanojunctions. Moreover, the charge transport in molecules at optical frequencies is a complex process affected by the interplay of multiple physical effects. A thorough investigation of electron transport mechanisms in molecules at optical frequencies requires theoretical and experimental efforts that go beyond the scope of this work. In spite of this, our study provides new insights into the physics of charge transport mechanisms across molecular junctions at optical frequencies via plasmon enhanced spectroscopy. We envision that combining the TPL non-linear spectroscopy technique with

an advanced theory of quantum charge transport as well as other electrical and optical characterization techniques could further advance our knowledge pertaining to the charge transport in conductive molecules at optical frequencies.

Author contributions: All the authors have accepted responsibility for the entire content of this submitted manuscript and approved submission.

Research funding: We acknowledge the financial support by the Research Grants Council of Hong Kong (GRF grant no. 15303417), the National Natural Science Foundation of China (Grant Nos. 12004273, 62022001 and 11704158), the China Postdoctoral Science Foundation (2018M630356), the European Research Council (ERC, Grant No. ERC-2014-CoG-648328), and the China Scholarship Council (CSC).

Conflict of interest statement: The authors declare no conflicts of interest regarding this article.

References

[1] D. Xiang, X. Wang, C. Jia, T. Lee, and X. Guo, "Molecular-scale electronics: from concept to function," *Chem. Rev.*, vol. 116, pp. 4318–4440, 2016.

[2] J. C. Cuevas and E. Scheer, *Molecular Electronics: An Introduction to Theory and Experiment*, USA, World Scientific Publishing Co, 2010.

[3] B. Q. Xu and N. J. Tao, "Measurement of single-molecule resistance by repeated formation of molecular junctions," *Science*, vol. 301, pp. 1221–1223, 2003.

[4] F. Chen, J. Hihath, Z. Huang, X. Li, and N. J. Tao, "Measurement of single-molecule conductance," *Annu. Rev. Phys. Chem.*, vol. 58, pp. 535–564, 2007.

[5] M. Galperin, M. A. Ratner, and A. Nitzan, "Inelastic electron tunneling spectroscopy in molecular junctions: peaks and dips," *J. Chem. Phys.*, vol. 121, pp. 11965–11979, 2004.

[6] S. H. Choi, B. S. Kim, and C. D. Frisbie, "Electrical resistance of long conjugated molecular wires," *Science*, vol. 320, pp. 1482–1486, 2008.

[7] L. Luo, A. Benameur, P. Brignou, S. H. Choi, S. Rigaut, and C. D. Frisbie, "Length and temperature dependent conduction of ruthenium-containing redox-active molecular wires," *J. Phys. Chem. C*, vol. 115, pp. 19955–19961, 2011.

[8] J. M. Beebe, B. S. Kim, C. D. Frisbie, and J. G. Kushmerick, "Measuring relative barrier heights in molecular electronic junctions with transition voltage spectroscopy," *ACS Nano*, vol. 2, pp. 827–832, 2008.

[9] N. Darwish, I. Díez-Pérez, P. Da Silva, N. Tao, J. J. Gooding, and M. N. Paddon-Row, "Observation of electrochemically controlled quantum interference in a single anthraquinone-based norbornylogous bridge molecule," *Angew. Chem. Int. Ed.*, vol. 51, pp. 3203–3206, 2012.

[10] V. Madhavan, W. Chen, T. Jamneala, M. F. Crommie, and N. S. Wingreen, "Tunneling into a single magnetic atom: spectroscopic evidence of the Kondo resonance," *Science*, vol. 280, pp. 567–569, 1998.

[11] D. Xu, X. Xiong, L. Wu, et al., "Quantum plasmonics: new opportunity in fundamental and applied photonics," *Adv. Opt. Photonics*, vol. 10, pp. 703–756, 2018.

[12] Z.-K. Zhou, J. Liu, Y. Bao, et al., "Quantum plasmonics get applied," *Pro. Quant. Electron.*, vol. 65, pp. 1–20, 2019.

[13] W. Chen, S. Zhang, M. Kang, et al., "Probing the limits of plasmonic enhancement using a two-dimensional atomic crystal probe," *Light Sci. Appl.*, vol. 7, p. 56, 2018.

[14] W. Zhu, R. Esteban, A. G. Borisov, et al., "Quantum mechanical effects in plasmonic structures with subnanometre gaps," *Nat. Commun.*, vol. 7, p. 11495, 2016.

[15] C. Ciracì, R. T. Hill, J. J. Mock, et al., "Probing the ultimate limits of plasmonic enhancement," *Science*, vol. 337, pp. 1072–1074, 2012.

[16] A. Reserbat-Plantey, I. Epstein, I. Torre, et al., "Quantum nanophotonics in two-dimensional materials," *ACS Photonics*, vol. 8, pp. 85–101, 2021.

[17] C. Vericat, M. E. Vela, G. Benitez, P. Carro, and R. C. Salvarezza, "Self-assembled monolayers of thiols and dithiols on gold: new challenges for a well-known system," *Chem. Soc. Rev.*, vol. 39, pp. 1805–1834, 2010.

[18] T. Wang and C. A. Nijhuis, "Molecular electronic plasmonics," *Appl. Mater. Today*, vol. 3, pp. 73–86, 2016.

[19] J.-C. Laroix, Q. V. Nguyen, Y. Ai, Q. V. Nguyen, P. Martin, and P.-C. Lacaze, "From active plasmonic devices to plasmonic molecular electronics," *Polym. Int.*, vol. 68, pp. 607–619, 2019.

[20] J. K. Viljas, F. Pauly, and J. C. Cuevas, "Modeling elastic and photoassisted transport in organic molecular wires: length dependence and current–voltage characteristics," *Phys. Rev. B*, vol. 77, p. 155119, 2008.

[21] Z.-C. Dong, X.-L. Guo, A. S. Trifonov, et al., "Vibrationally resolved fluorescence from organic molecules near metal surfaces in a scanning tunneling microscope," *Phys. Rev. Lett.*, vol. 92, p. 086801, 2004.

[22] H. Shan, Y. Yu, X. Wang, et al., "Direct observation of ultrafast plasmonic hot electron transfer in the strong coupling regime," *Light Sci. Appl.*, vol. 8, p. 9, 2019.

[23] M. Galperin, A. Nitzan, and M. A. Ratner, "Molecular transport junctions: current from electronic excitations in the leads," *Phys. Rev. Lett.*, vol. 96, p. 166803, 2006.

[24] T. Frederiksen, M. Brandbyge, N. Lorente, and A.-P. Jauho, "Inelastic scattering and local heating in atomic gold wires," *Phys. Rev. Lett.*, vol. 93, p. 256601, 2004.

[25] W. Zhang, H. Liu, J. Lu, et al., "Atomic switches of metallic point contacts by plasmonic heating," *Light Sci. Appl.*, vol. 8, p. 34, 2019.

[26] J. A. Scholl, A. García-Etxarri, A. L. Koh, and J. A. Dionne, "Observation of quantum tunneling between two plasmonic nanoparticles," *Nano Lett.*, vol. 13, pp. 564–569, 2013.

[27] K. J. Savage, M. M. Hawkeye, R. Esteban, A. G. Borisov, J. Aizpurua, and J. J. Baumberg, "Revealing the quantum regime in tunnelling plasmonics," *Nature*, vol. 491, pp. 574–577, 2012.

[28] O. Pérez-González, N. Zabala, A. G. Borisov, N. J. Halas, P. Nordlander, and J. Aizpurua, "Optical spectroscopy of conductive junctions in plasmonic cavities," *Nano Lett.*, vol. 10, pp. 3090–3095, 2010.

[29] F. Benz, C. Tserkezis, L. O. Herrmann, et al., "Nanooptics of molecular-shunted plasmonic nanojunctions," *Nano Lett.*, vol. 15, pp. 669–674, 2015.
[30] D. Knebl, A. Hörl, A. Trügler, et al., "Gap plasmonics of silver nanocube dimers," *Phys. Rev. B*, vol. 93, p. 081405(R), 2016.
[31] Q. Zhang, X. Cai, X. Yu, et al., "Electron energy-loss spectroscopy of spatial nonlocality and quantum tunneling effects in the bright and dark plasmon modes of gold nanosphere dimers," *Adv. Quantum Technol.*, vol. 1, p. 1800016, 2018.
[32] X. Cui, F. Qin, Y. Lai, et al., "Molecular tunnel junction-controlled high-order charge transfer plasmon and fano resonances," *ACS Nano*, vol. 12, pp. 12541–12550, 2018.
[33] S. F. Tan, L. Wu, J. K. W. Yang, P. Bai, M. Bosman, and C. A. Nijhuis, "Quantum plasmon resonances controlled by molecular tunnel junctions," *Science*, vol. 343, pp. 1496–1499, 2014.
[34] R. Bardhan, S. Mukherjee, N. A. Mirin, S. D. Levit, P. Nordlander, and N. J. Halas, "Nanosphere-in-a-nanoshell: a simple nanomatryushka," *J. Phys. Chem. C*, vol. 114, pp. 7378–7383, 2010.
[35] J. Song, B. Duan, C. Wang, et al., "SERS-encoded nanogapped plasmonic nanoparticles: growth of metallic nanoshell by templating redox-active polymer brushes," *J. Am. Chem. Soc.*, vol. 136, pp. 6838–6841, 2014.
[36] W. Shen, X. Lin, C. Jiang, et al, "Reliable quantitative SERS analysis facilitated by core–shell nanoparticles with embedded internal standards," *Angew. Chem. Int. Ed.*, vol. 54, pp. 7308–7312, 2015.
[37] N. G. Khlebtsov, L. Lin, B. N. Khlebtsov, and J. Ye, "Gap-enhanced Raman tags: fabrication, optical properties, and theranostic applications," *Theranostics*, vol. 10, pp. 2067–2094, 2020.
[38] L. Lin, M. Zapata, M. Xiong, et al., "Nanooptics of plasmonic nanomatryoshkas: shrinking the size of a core–shell junction to subnanometer," *Nano Lett.*, vol. 15, pp. 6419–6428, 2015.
[39] M. Khalid and C. Ciracì, "Numerical analysis of nonlocal optical response of metallic nanoshells," *Photonics*, vol. 6, p. 39, 2019.
[40] M. Zapata, Á. S. Camacho Beltrán, A. G. Borisov, and J. Aizpurua, "Quantum effects in the optical response of extended plasmonic gaps: validation of the quantum corrected model in core–shell nanomatryushkas," *Opt. Express*, vol. 23, pp. 8134–8149, 2015.
[41] M. Khalid, F. D. Sala, and C. Ciracì, "Optical properties of plasmonic core–shell nanomatryoshkas: a quantum hydrodynamic analysis," *Opt. Express*, vol. 26, pp. 17322–17334, 2018.
[42] V. Kulkarni, E. Prodan, and P. Nordlander, "Quantum plasmonics: optical properties of a nanomatryushka," *Nano Lett.*, vol. 13, pp. 5873–5879, 2013.
[43] D. Liu, T. Wu, Q. Zhang, et al., "Probing the in-plane near-field enhancement limit in a plasmonic particle-on-film nanocavity with surface-enhanced Raman spectroscopy of graphene," *ACS Nano*, vol. 13, pp. 7644–7654, 2019.
[44] L. Lin, Q. Zhang, X. Li, et al., "Electron transport across plasmonic molecular nanogaps interrogated with surface-enhanced Raman scattering," *ACS Nano*, vol. 12, pp. 6492–6503, 2018.
[45] W. Zhu and K. B. Crozier, "Quantum mechanical limit to plasmonic enhancement as observed by surface-enhanced Raman scattering," *Nat. Commun.*, vol. 5, p. 5228, 2014.
[46] G. Hajisalem, M. S. Nezami, and R. Gordon, "Probing the quantum tunneling limit of plasmonic enhancement by third harmonic generation," *Nano Lett.*, vol. 14, pp. 6651–6654, 2014.
[47] L. Lin, H. Gu, and J. Ye, "Plasmonic multi-shell nanomatryoshka particles as highly tunable SERS tags with built-in reporters," *Chem. Commun.*, vol. 51, pp. 17740–17743, 2015.
[48] L. Lin, Z. Liu, X. Li, H. Gu, and J. Ye, "Quantifying the reflective index of nanometer-thick thiolated molecular layers on nanoparticles," *Nanoscale*, vol. 9, pp. 2213–2218, 2017.
[49] P. B. Johnson and R. W. Christy, "Optical constants of the noble metals," *Phys. Rev. B*, vol. 6, p. 4370, 1972.
[50] C. F. Bohren and D. R. Huffman, *Absorption and Scattering of Light by Small Particles*, Berlin, Wiley-VCH, 2008.
[51] G.-C. Li, Y.-L. Zhang, J. Jiang, Y. Luo, and D. Y. Lei, "Metal-substrate-mediated plasmon hybridization in a nanoparticle dimer for photoluminescence line-width shrinking and intensity enhancement," *ACS Nano*, vol. 11, pp. 3067–3080, 2017.
[52] D.-S. Wang, F.-Y. Hsu, and C.-W. Lin, "Surface plasmon effects on two photon luminescence of gold nanorods," *Opt. Express*, vol. 17, pp. 11350–11359, 2009.
[53] L. Chen, G.-C. Li, G.-Y. Liu, et al., "Sensing the moving direction, position, size, and material type of nanoparticles with the two-photon-induced luminescence of a single gold nanorod," *J. Phys. Chem. C*, vol. 117, pp. 20146–20153, 2013.
[54] Z. Huang, Q. Dai, S. Lan, and S. Tie, "Numerical study of nanoparticle sensors based on the detection of the two-photon-induced luminescence of gold nanorod antennas," *Plasmonics*, vol. 9, pp. 1491–1500, 2014.
[55] G. T. Boyd, Z. H. Yu, and Y. R. Shen, "Photoinduced luminescence from the noble metals and its enhancement on roughened surfaces," *Phys. Rev. B*, vol. 33, pp. 7923–7936, 1986.
[56] R. Esteban, A. G. Borisov, P. Nordlander, and J. Aizpurua, "Bridging quantum and classical plasmonics with a quantum-corrected model," *Nat. Commun.*, vol. 3, p. 825, 2012.
[57] J. W. You and N. C. Panoiu, "Analysis of the interaction between classical and quantum plasmons via FDTD–TDDFT method," *IEEE J. Multisc. Multiphys. Comput. Technol.*, vol. 4, pp. 111–118, 2019.
[58] B. Gerislioglu and A. Ahmadivand, "Functional charge transfer plasmon metadevices," *Research*, vol. 2020, p. 9468692, 2020.
[59] C. Jia and X. Guo, "Molecule–electrode interfaces in molecular electronic devices," *Chem. Soc. Rev.*, vol. 42, pp. 5642–5660, 2013.
[60] R. L. McCreery and A. J. Bergren, "Progress with molecular electronic junctions: meeting experimental challenges in design and fabrication," *Adv. Mater.*, vol. 21, pp. 4303–4322, 2009.
[61] Q. Lu, K. Liu, H. Zhang, Z. Du, X. Wang, and F. Wang, "From tunneling to hopping: a comprehensive investigation of charge transport mechanism in molecular junctions based on oligo(*p*-phenylene ethynylene)s," *ACS Nano*, vol. 3, pp. 3861–3868, 2009.

Supplementary Material: The online version of this article offers supplementary material (https://doi.org/10.1515/nanoph-2021-0116).